PAPER

On the design of piezoelectric actuator for 1D MEMS scanning mirror applications

To cite this article: Shih-Chi Liu *et al* 2023 *J. Micromech. Microeng.* **33** 034002

View the article online for updates and enhancements.

On the design of piezoelectric actuator for 1D MEMS scanning mirror applications

Shih-Chi Liu[1]**, Hao-Chien Cheng**[2]**, Si-Han Chen**[1]**, Hung-Yu Lin**[1]**, Chih-Chen Hsu**[1]**, Fuchi Shih**[2]**, Kai-Chih Liang**[3]**, Mingching Wu**[3] **and Weileun Fang**[1,2,*]

[1] Department of Power Mech. Engineering, National Tsing Hua University, Hsinchu City, Taiwan
[2] Institution of NanoEng. and Microsyst., National Tsing Hua University, Hsinchu City, Taiwan
[3] Coretronic MEMS Corporation, Hsinchu, Taiwan

E-mail: fang@pme.nthu.edu.tw

CrossMark

Abstract

This study presents the design, implementation, and characterization of 1D resonant type micro-electro-mechanical-systems (MEMS) piezoelectric scanning mirrors with different actuator designs to investigate their influences on the figure of merits (FoMs) for automotive light detection and ranging application. The MEMS scanning mirrors are driven by lead zirconate titanate (PZT) thin film in this study owing to its outstanding piezoelectric properties. Three different beam-type piezoelectric actuators are designed, including the reference meander straight-beam actuator design, and the proposed meander curved-beam and straight-curved tapered beam actuator designs. Simulations show the scan angle enhancement for two proposed designs, yet the resonant scanning frequency of meander curved-beam design dropped to below the 2 kHz requirement. To evaluate the designs, scanning mirrors with two proposed actuators are fabricated and tested. Measurements show that the resonant frequencies for the two proposed MEMS scanning mirrors are 1735 Hz and 2578 Hz, respectively. Two proposed designs respectively have the maximum optical angles of 48.1° and 50.6° at the 20 V_{pp} driving voltage. Due to the much higher stress on the beam structure induced by the misalignment of PZT film, the actuator could not reach the predicted scanning angle of near 80°. In comparison of the two proposed designs, the straight-curved tapered beam actuator design could enhance the FoM for about 56%. In summary, the performances of piezoelectric MEMS scanning mirror can be improved by varying the designs of length and shape of actuator, and the distribution of PZT film on the suspended actuator is also a critical design concern.

Supplementary material for this article is available online

Keywords: MEMS, scanning mirror, piezoelectric actuator, PZT film, LiDAR

(Some figures may appear in colour only in the online journal)

1. Introduction

The micro-electro-mechanical-systems (MEMS) scanning mirrors have been applied in various fields such as light detection and ranging (LiDAR) system [1], augmented reality [2], laser display, and medical imaging [3, 4]. Among these fields, the LiDAR system can achieve three-dimensional configuration mapping in a short duration with high resolution, which is the key enabling technology for future autonomous driving applications. Compared with other LiDAR technologies such as motorized scanner [5], flash light [6], and

---

* Author to whom any correspondence should be addressed.

optical-phase-array scanner [7], MEMS scanning mirrors offer the advantages of high resolution, fast response, and small size. In addition, by leveraging the characteristics of batch production for micromachining processes, the cost of MEMS scanning mirrors can be reduced. Therefore, the miniaturized LiDAR system with MEMS scanning mirror as its scanner is a highly competitive option. As a LiDAR module, the design of MEMS LiDAR has to consider three critical figures of merit, including scanning frequency, scanning angle, and mirror size, which correspond to data collection rate, field of view, and the maximum detecting distance, respectively.

In general, the electrostatic, electromagnetic, and piezo-electric are three driving mechanisms for MEMS scanning mirrors. The electrostatic actuations through parallel plates, comb electrodes, etc, have been extensively applied to drive MEMS scanning mirrors. The power consumption for electrostatic MEMS scanning mirror is low and the fabrication processes are highly compatible with the existing technologies. However, the actuation voltage usually exceeds 100 V [8–10], which is a critical concern in many applications. The driving voltage could be lowered by reducing the gap between electrodes, however the pull-in effect is another concern, especially for the automotive applications. The electromagnetic actuation could offer a large driving force (Lorentz force) to the MEMS scanning mirror to achieve a large deflection angle [3, 11, 12]. However, the extra assembly process for the magnets is still a challenge toward low cost and batch production, and the package size would be magnified because of the bulky magnets. Moreover, the joule heat generated by the coil during driving may accelerate the aging of devices. In recent years, the piezoelectric actuation has been adopted in many MEMS devices, such as microphones [13], microspeakers [14], and micro scanning mirrors [15–21]. The characteristics of piezo-electric thin films have been exploited to deform the suspended micro structures by using the electric field, so that the micro scanning mirrors can be excited. The piezoelectric actuation offers the advantages of low power consumption and large driving force in a more compact chip size, making it a promising mechanism for realizing MEMS actuators. Due to the superior piezoelectric material properties, the lead zirconate titanate (PZT) shows outstanding driving force for actuator applications, as compared with other piezoelectric films such as AlN, ZnO, etc. Thus, this study will employ the PZT thin film to design and implement the micro scanning scanner for MEMS LiDAR.

For automotive application, the components with moving parts are frequently under excitations within the frequency range of 20–2000 Hz range [22]. Thus, the scanning frequency of the MEMS scanning mirror should be avoided in this range. However, it is challenging to design the piezoelectric MEMS scanner with a large mirror plate having a resonant scanning mode above 2 kHz and a decent scanning angle. Several previous studies have dedicated to realize MEMS mirror devices for automotive LiDAR applications [23, 24], yet the scanning frequency is still lower than 2 kHz. In this study, MEMS scanners with a 3 mm diameter mirror plate and a resonant scanning mode above 2 kHz will be designed and implemented,

and the piezoelectric cantilever actuator designs are investigated to achieve the performance enhancement. In general, the output displacement and stiffness of the piezoelectric cantilever actuator are significantly influenced by the shape and equivalent length of the beam. Thus, under a given chip size, this study presents a reference and two proposed designs of the cantilever actuators to find the solution for scan angle enhancement. The characteristics of these three designs are evaluated by simulations first, and then the proposed MEMS scanning mirrors are fabricated and tested to demonstrate their performances.

2. Design concept

The working principle of a piezoelectric unimorph micro actuator is depicted in figure 1. The suspended laminated structure is consisted of the piezoelectric thin film on the top of a micromachined cantilever (in this study, it is Si). As indicated in figure 1(a), the beam length is L, and the thicknesses of piezoelectric and Si layers are respectively t_p and t_{si}. As the piezoelectric material is driven by an out-of-plane electric field E_3 generated by the input driving voltage V, an in-plane strain ε_1 will be induced based on the inverse piezoelectric effect, which can be expressed as,

$$\varepsilon_1 = d_{31}E_3 \tag{1}$$

where d_{31} is the transverse piezoelectric coefficient of piezoelectric material. The subscripts 1 and 3 illustrate the causation between the applied electric field and the induced strain. After that, as shown in figure 1(b), the unimorph structure will be bent up or down according to the bias voltage, thereby providing a tip displacement δ_{st}, which can be expressed as [25],

$$\delta_{st} = \frac{3d_{31}s_{si}s_p t_{si}(t_{si}+t_p)L^2 V}{s_{si}^2 t_p^4 + 4s_{si}s_p t_{si}t_p^3 + 6s_{si}s_p t_{si}^2 t_p^2 + 4s_{si}s_p t_{si}^3 t_p + s_p^2 t_{si}^4} \tag{2}$$

where s_{si} and s_p are respectively the compliance of the micromachined Si cantilever and the piezoelectric film. According to equation (2), the tip displacement of a piezoelectric cantilever actuator is proportional to the transverse piezoelectric coefficient, length of the beam, and driving voltage on the assumption that the thickness and compliance of silicon and piezoelectric material are constant. Note that the equation (2) is only valid when there is no reaction force applied on the actuator. However, the mirror plate will apply a reaction force on the actuator during scanning. Thus, the stiffness of the actuator is another design concern to increase the angular deflection of mirror.

Figure 2 illustrates the schematic drawing of the reference and two proposed MEMS scanning mirror designs. The proposed scanning mirrors are fabricated on the SOI (silicon on insulator) wafer. The size of mirror and the footprint of the chip are the same for these three designs. As indicated in figures, the scanning mirror consists of a circular mirror plate, two torsional springs, and four piezoelectric actuators.
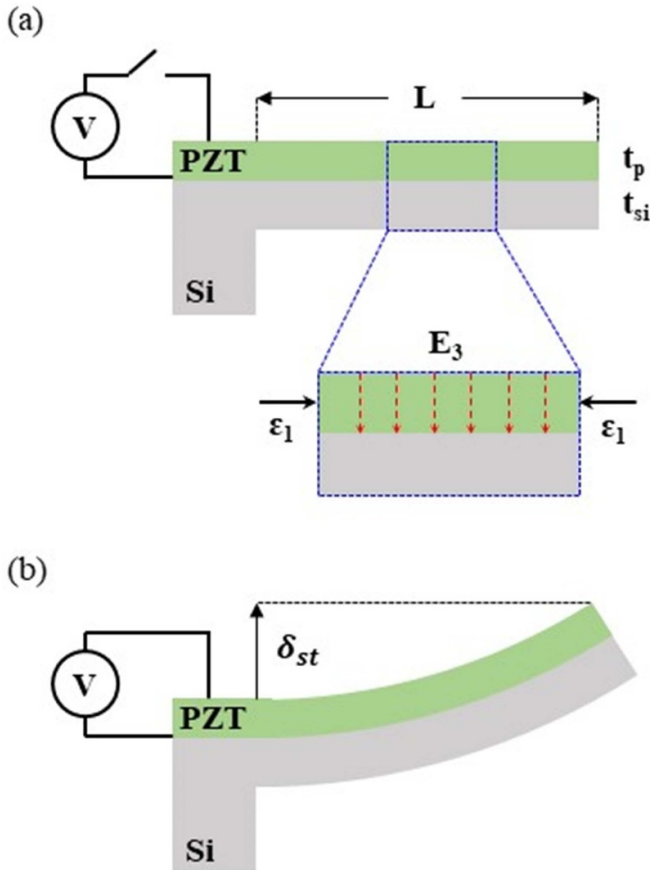
Figure 1. (a) Schematic drawing of the piezoelectric unimorph cantilever actuator consisted of the Si device layer and PZT thin film, (b) cantilever bending induced by the inverse piezoelectric effect.

The torsional spring and piezoelectric actuator are anchored to the substrate. The mirror plate which supported by two torsional springs is driven by four piezoelectric actuators, so that the mirror plate could rotate about torsional springs for optical scanning. According to optical design considerations, the diameter of mirror plate is 3 mm. In this study, three different beam-type actuator designs together with the associated top electrodes will be investigated. Figure 2(a) presents the reference scanning mirror with the meander straight-beam actuator design. As depicted in the zoom-in schematic illustration, the actuator is a meander structure consisted of two straight beams. One end of the meander straight-beam actuator is anchored to the substrate whereas another end is connected to the mirror plate. The length of the meander straight-beam actuator is determined by the backside opening of the chip. This study also employs the dual-electrode design in [14] for the driving electrode of each straight-beam. Thus, the meander straight-beam actuator can be deformed in a preferred shape (i.e. the deformed beam existing two different curvatures). The torsional springs are employed to modulate the scanning frequency and also to increase the stiffness in the out-of-plane direction to avoid the piston motion during driving. Moreover,

as displayed by the cross-section illustration, to enable large scanning motion of the mirror, the substrate under the scanning mirror will be removed. However, part of the substrate is reserved to act as the rib structure (80 μm thick and 120 μm wide) to enhance the stiffness of the mirror plate [26, 27]. Thus, the dynamic deformation of the mirror plate is suppressed. To make a fair comparison between these three actuator designs, the pattern and dimension of the rib structure on the mirror plate are identical.

To increase the length as well as the output displacement of the actuator, this study presents the meander curved-beam actuator design, as illustrated in figure 2(b). As displayed in the zoom-in schematic illustration, the curved-beam is designed to distribute along the circumference of the mirror plate. Thus, the circumference of the circular mirror plate is surrounded by four meander curved-beam actuators. Each actuator is consisted of two curved beams. The dual-electrode design is also used for the driving electrode of each curved-beam. To evaluate the influence of actuators on the scanning characteristics of the mirror, this design has the same torsional springs as those in figure 2(a). This study also presents the design in figure 2(c) to not only increase the length but also modulate the stiffness of the actuator. As displayed in the zoom-in illustration, this design exploits the straight-curved tapered beam as the actuator to boost the stiffness of the beam structure. The stiffness of the straight-curved tapered beam can easily be modulated by varying the shape of tapered beam. The dual-electrode designs are employed for both the straight part and curved part of the tapered beam. Note that the dimensions of torsional springs could be used to lower the resonant frequency of scanning mode for mirror.

The commercial finite element method (FEM) software is used to predict the characteristics of the proposed and reference mirror designs. Figure 3 depicts simulation results of resonant frequencies and the related resonant modes for these three designs. The simulations were done by eigenfrequency analysis in the software, and the structures have the clamped boundary condition at their anchors (as indicated in figure). Table 1 lists important material parameters used in simulations. The results depict that the first mode of these three designs are all torsional mode (i.e. optical scanning mode) which could fulfill the requirement of optical scanner. Simulations also demonstrate the deforming beams of each actuator have two different curvatures, thus justifying the design of dual-electrode. Moreover, the first resonant frequencies for these three designs are respectively 2334 Hz (meander straight-beam), 1673 Hz (meander curved-beam), and 2065 Hz (straight-curved tapered beam). It indicates the scanning mode resonant frequency is dropped below the 2 kHz requirement due to the low stiffness of meander curved-beam design. By using the tapered beam design in figure 2(c), the resonant frequency of scanning mode is back to above 2 kHz. This study further investigates the mechanical angles of these three mirror designs when driven at their 1st resonant frequencies through the 'frequency domain analysis' provided by the FEM software. The key parameters employed in the dynamic

(a) Reference type

(b) Meander curved-beam type

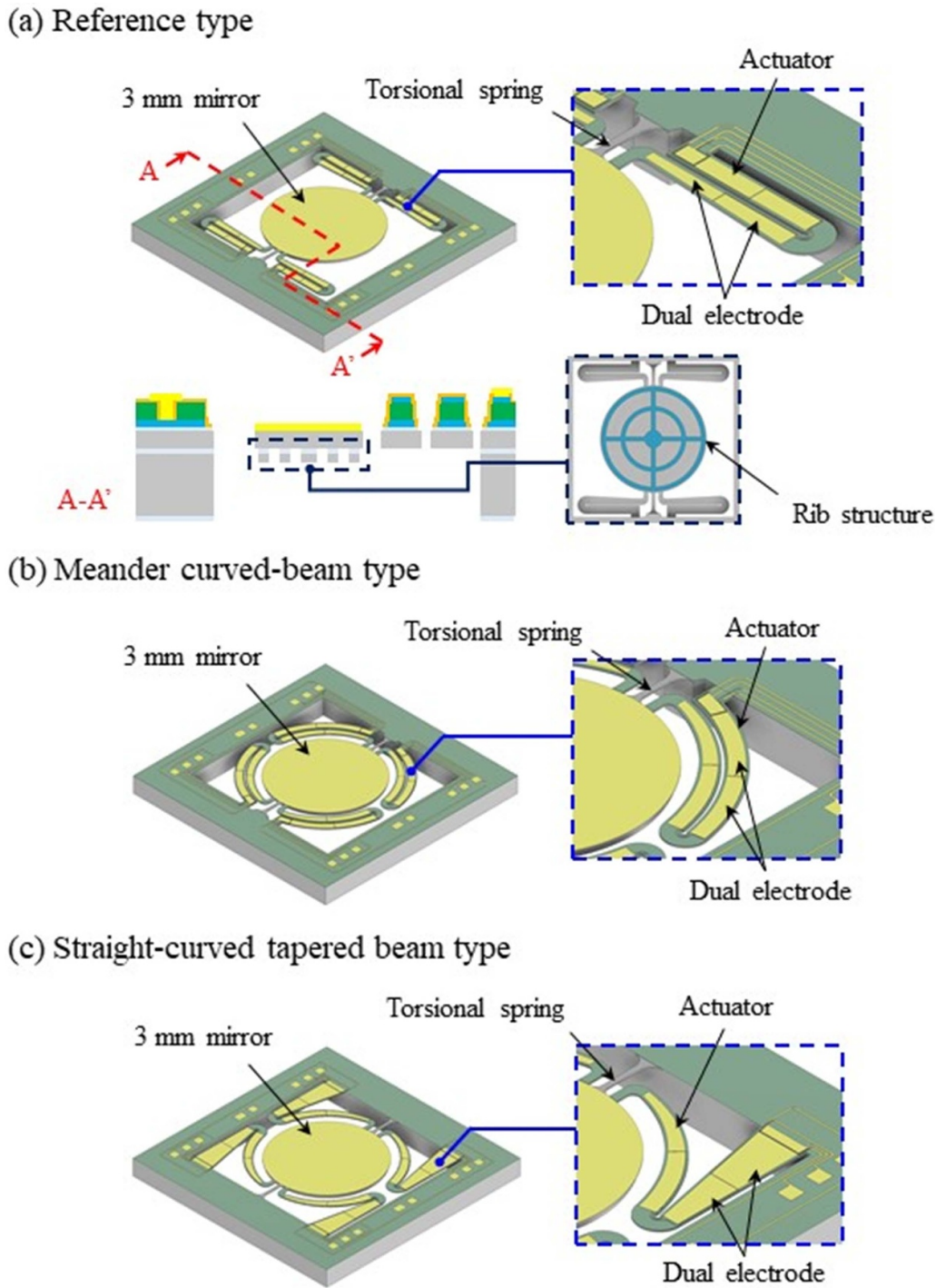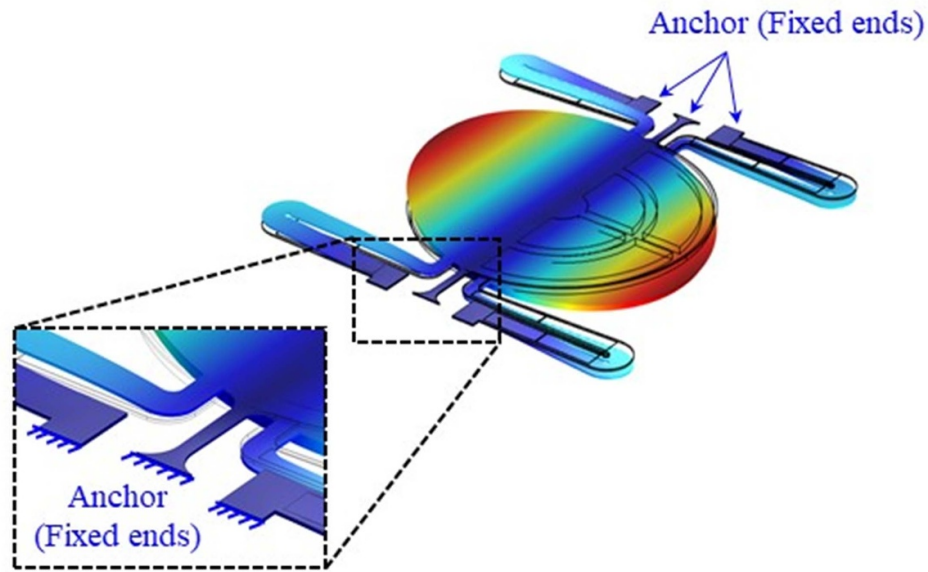## (c) Straight-curved tapered beam type

Figure 2. Schematic illustrations of the piezoelectric MEMS scanning mirrors with, (a) the reference meander straight-beam actuators, (b) the proposed meander curved-beam actuators, (c) the proposed straight-curved tapered beam actuators.

response simulation include the piezoelectric coefficient of PZT d_{31}, and the quality factor, as summarized in table 1. For a conservative estimate, the d_{31} and quality factor were set -70 pm V^{-1} and 125, respectively. Simulations in figure 4 exhibit the relationship between driving voltages and mechanical angles of these three mirror designs. The largest mechanical angle for each design is limited by the maximum allowable stress of Si structure employed in this study (1.2 GPa after

considering the safety factor for operating environment). The results indicate the reference mirror design (meander straight-beam) has a maximum mechanical angle of $\pm 20.2°$ when driven at 47 V$_{pp}$. For proposed scanners, the one with meander curved-beam design has a maximum mechanical angle of $\pm 20°$ (at 31 V$_{pp}$), and the one with straight-curved tapered beam design has a maximum mechanical angle of $\pm 19.8°$ (at 30 V$_{pp}$). As compare with the reference design, both proposed
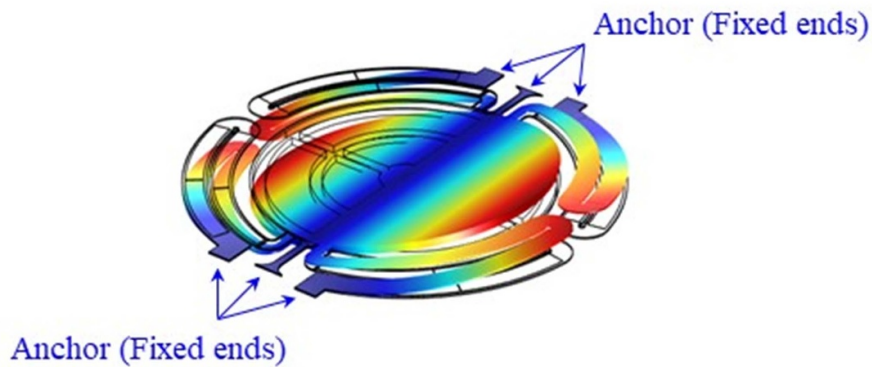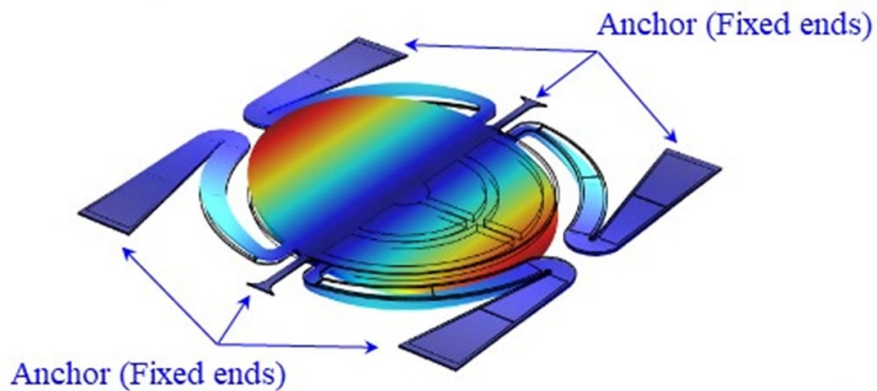
Figure 3. The scanning mode shape and the related resonant frequencies, (a) the reference design, (b) the proposed meander curved-beam design, (c) the proposed straight-curved tapered beam design.

designs show comparable mechanical angle with reduced driving voltages. In summary, the meander curved-beam design could increase the length of actuator to enhance the mechanical angle. However, the stiffness of the actuator is decreased so as to lower the natural frequency (scanning mode) of the scanner. Thus, the proposed design with straight-curved tapered beam actuator could improve the natural frequency to meet the 2 kHz requirement while maintaining the scan angle.

Table 1. Material parameters used in the FEM simulation.

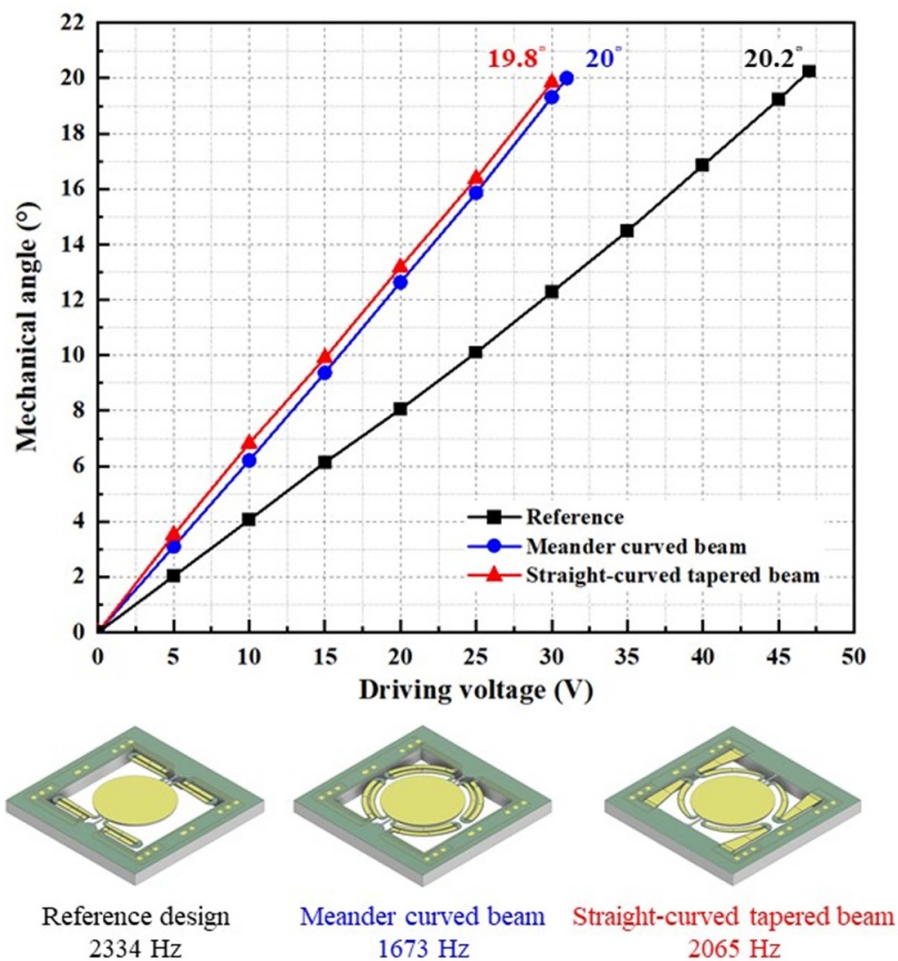| Parameters	Silicon	PZT-5A
Layer thickness h (μm)	15	5
Young's modulus E (GPa)	170	60
Poisson ratio γ	0.3	0.28
Density ρ (kg/m^3)	2500	7600
Piezoelectric coefficient d_{31} (pm/V)	N/A	-70
Isotropic loss factor ξ (Quality factor Q = 1/2ξ)	0.004 (Q = 125)	0.004 (Q = 125)

Figure 4. Simulation results for the mechanical angles of reference and proposed MEMS scanning mirror designs at their scanning mode frequency with respect to the maximum allowable stress of Si structure, (a) the reference design, (b) the proposed meander curved-beam actuators, (c) the proposed straight-curved tapered beam actuators.
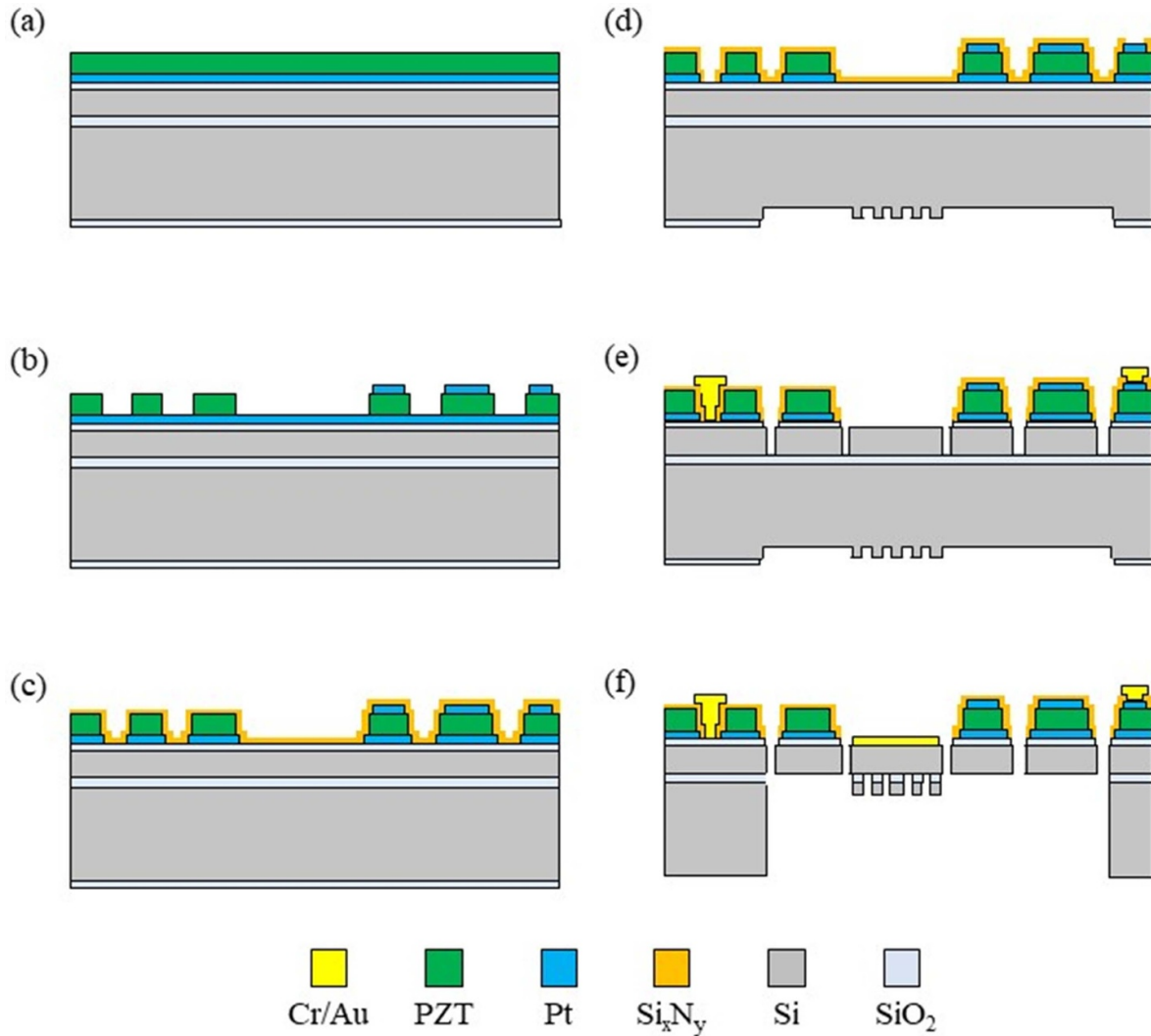
Figure 5. Fabrication processes for the proposed MEMS scanning mirror, (a) SOI wafer with thermal oxide, Pt bottom electrode, and PZT film, (b) Pt top electrode and PZT film patterned by RIE, (c) Pt bottom electrode patterned by RIE and then encapsulated by PECVD nitride, (d) backside Si patterned by DRIE to define ribs and front side nitride opened to define contact areas, (e) Au metal contact lift-off and front side Si device layer patterned by DRIE to define scanner, and (f) handle Si layer etched by DRIE and then release the structure by removing the buried oxide layer, and Au reflecting layer deposited through a shadow mask.

3. Fabrication and results

The fabrication processes for the proposed MEMS scanning mirror are depicted in figure 5. As shown in figure 5(a), the Pt bottom electrode layer and the PZT film (5 μm) were deposited on the SOI wafer with a 15 μm thick silicon device layer. As indicated in figure 5(b), the Pt top electrode layer was sputtered and then patterned by the reactive ion etching (RIE). After that, the PZT film was also patterned by the RIE. As illustrated in figure 5(c), after the Pt bottom electrode patterned by the RIE, a silicon nitride thin film was deposited by plasma enhanced chemical vapor deposition (PECVD) to form passivation layer to prevent the PZT thin film from affecting by moisture. Figure 5(d) shows that the backside thermal oxide was patterned and then the shape of ribs was defined by the DRIE (deep RIE). Moreover, the PECVD nitride located on the electrical connection pad was removed for the following

metal pad lift-off process to enable the electrical connection. As depicted in figure 5(e), the frontside oxide and nitride layers were patterned by the RIE, and then the device silicon layer was etched by the DRIE to define the whole mirror structure. As shown in figure 5(f), the backside silicon was etched to form ribs under the mirror plate, then the buried oxide was removed to release structures from substrate. Finally, the metal reflection layer on the mirror was deposited through a shadow mask.

The SEM (scanning electron microscopy) micrographs in figure 6 present the fabricated piezoelectric MEMS scanning mirrors. Micrographs in figures 6(a) and (b) respectively show two proposed MEMS scanning mirror with different beam-type actuator designs. The footprint of chip is 6.4 mm $\times$ 6.4 mm and the diameter of the mirror plate is 3 mm. The zoom-in micrographs in figures 6(c) and (d) further display the meander curved-beam and straight-curved tapered
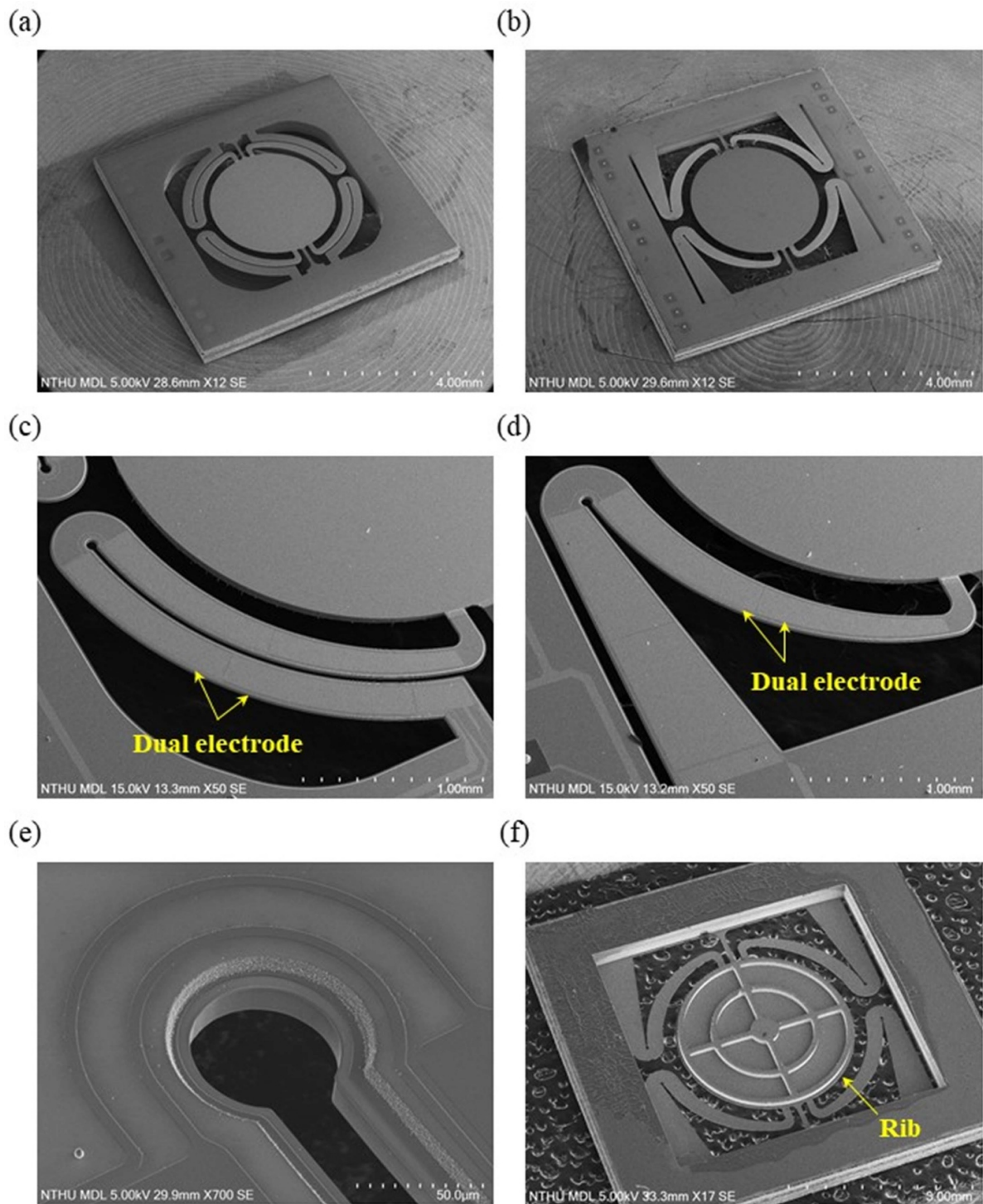
Figure 6. The SEM micrographs of typical fabricated MEMS scanning mirrors. The chips with scanners having (a) the meander curved-beam design, and (b) the straight-curved tapered beam design; zoom-in micrographs to show (c) meander curved-beam actuator, (d) straight-curved tapered beam actuator; (e) round corner on structure to reduce stress; and (f) the backside view of the chip to show the rib reinforced structures on the mirror plate.

beam actuator designs. The round shape shown in figure 6(e) was patterned near the corner of meander beam structures to avoid the stress concentration. Micrograph in figure 6(f) exhibits the backside view of the chip, and the ribs to enhance the stiffness of mirror are observed. Moreover, rib profiles of the two fabricated MEMS scanning mirrors are measured by the

laser scanning confocal microscopy as shown in figure 7. The cross-sections depict typical surface topography of rib structures. Measurements indicate the width of the ribs is approximate 106 μm, and the thickness of ribs is approximate 90–100 μm. Finally, figure 8 shows the microscope images of two different fabricated MEMS scanning mirrors wire-bonded and
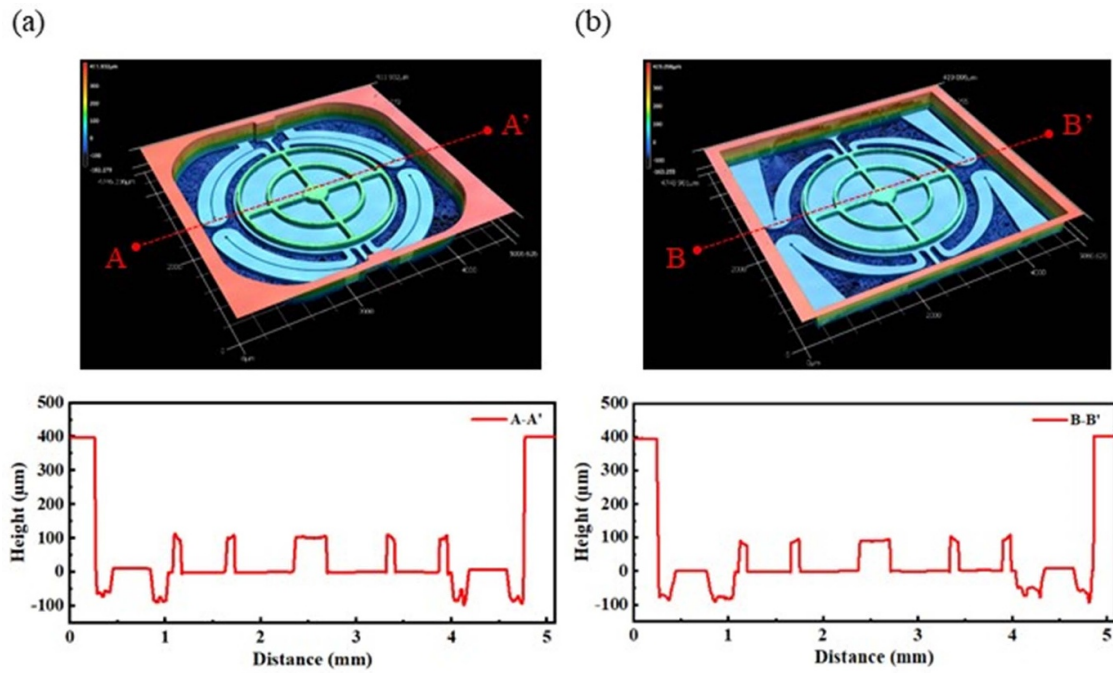
Figure 7. The 3D image and surface topography of backside rib structures measured using the laser confocal microscope, (a) meander curved-beam design, (d) straight-curved tapered beam design.
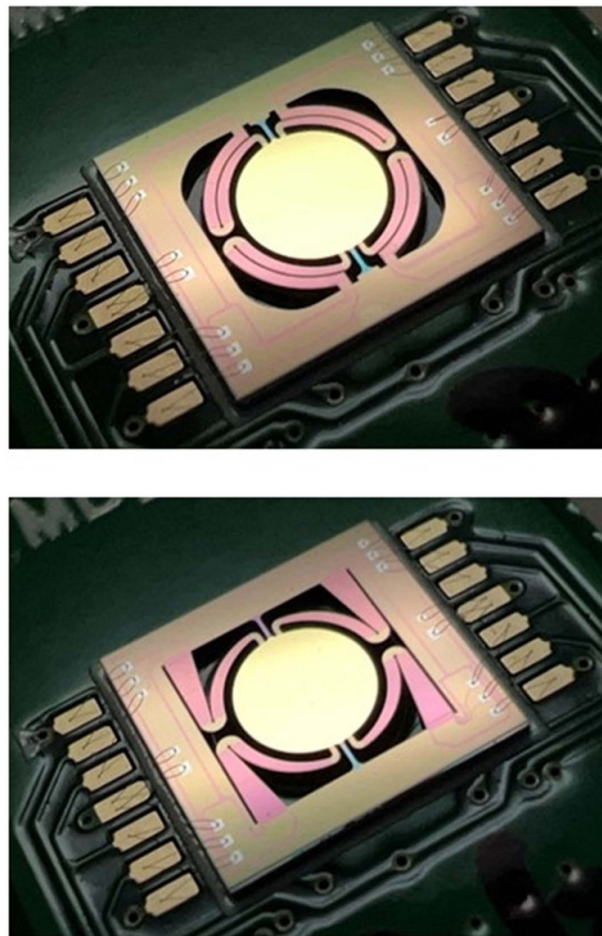

Figure 8. MEMS scanning mirror chips wire-bonding on the PCB as the device-under-test (DUT).

mounted on a printed circuit board (PCB) as the device-under-test (DUT). Note that the PCB has a hole beneath the mirror plate to avoid the effect of air damping during driving.

4. Measurement and results

This study has performed various experiments to characterize the material properties of PZT thin film, such as the transverse piezoelectric coefficient and ferroelectric hysteresis curve. In addition, this study has also measured the dynamic characteristics and performances of MEMS scanning mirrors, such as frequency response, resonant mode shape, and the optical scanning angle.

4.1. Material properties characterization for PZT film

The Sawyer–Tower circuit illustrated in figure 9(a) was utilized in this study to evaluate the variation of polarizations with applied electric fields (P–E curve) of PZT. The signal generator and power amplifier are employed to apply an electric field on the PZT test structure, and then the voltage output was measured by an oscilloscope. After that, the polarization of the PZT could be evaluated by

$$P = \frac{V_0 \times C_{\text{ref}}}{A} \tag{3}$$

where P is the polarization, V_0 is the voltage output, C_{ref} is the capacitance of reference capacitor, and A is the area of the test structure. Figure 9(b) shows measurement results with applied electric fields up to 100 kV cm^{-1}. The polarization under 100 kV cm^{-1} biasing is around 25 μC cm^{-2}, and the remnant polarization and coercive electric field are 7 μC cm^{-2} and 20 kV cm^{-1}, respectively. Moreover, this study also fabricated cantilevers consisted of PZT thin film and silicon device layer as the testkey to extract d_{31} coefficient. The load-deflection tests were adopted to measure the target piezoelectric coefficient, and the measurement set up is illustrated in figure 10(a). As a DC voltage input to the electrodes, the piezoelectric unimorph cantilever testkey would bend due to the inverse piezoelectric effect. The white light interferometry was employed to measure the tip displacement of the beams, and the piezoelectric coefficient is determined by equation (2). Figure 10(b) shows the measurement results of d_{31} coefficient as the input voltage changing back and forth between 5 V and 50 V. The d_{31} coefficients determined from cantilevers of different lengths show good agreement. Thus, the d_{31} coefficient of the PZT thin film is around -145 pm V^{-1}. Note that due to the remnant polarization phenomenon observed in the P–E curve measurement, the d_{31} coefficient measured from lower input voltage showed larger standard deviation.

4.2. Dynamic tests for MEMS scanning mirrors

Firstly, the resonant frequencies of presented MEMS scanning mirrors are measured using the commercial laser Doppler vibrometer, as illustrated in figure 11(a). The DUTs shown in figure 8 were fixed on a stage and driven with a 1 V$_{\text{pp}}$ periodic wave signal. Measurements in figures 11(b) and (c) depict typical frequency responses of the two proposed mirror designs. For meander curved-beam design, the resonant frequency of scanning mode is 1670 Hz, followed by three higher resonant modes within the frequency range of 1–4 kHz. For straight-curved tapered beam design, the resonant frequency of scanning mode is 2236 Hz, and there are no other resonant modes in the frequency range of 1 kHz to 4 kHz. Moreover, this study also employed the commercial digital hologram microscopy (DHM) to verify the resonant mode shape at the measured scanning frequencies. As shown in figure 12(a), the devices were driven by a 1 V$_{\text{pp}}$ unipolar sinusoidal signal at their scanning mode frequency generated from a stroboscopic unit. The DHM will capture the dynamic responses of the mirror at the given frequencies. Figures 12(b) and (c) show typical measurement results of scanning modes respectively for the presented two designs. As limited by the field of view of the microscope, the free end of the mirror plate and its connection to the torsional spring are displayed separately. Measurements depict the meander curved-beam actuator has significant movements during driving, as compare with the straight-curved tapered beam design. It indicates the straight-curved tapered beam design could consume less kinetic energy during the operation, so that the input energy at the scanning mode is mainly contributed to the rotation of mirror plate.

This study also establishes the test setup in figure 13(a) to measure the mechanical angle of presented MEMS mirrors. The laser was incident on the mirror plate of the DUT and then reflected onto a screen. When the DUT was electrical driven at its torsional frequency, the laser beam will be steered by the mirror plate, and consequently displaying a scanning trace on the screen. As a result, the mechanical angle of the MEMS mirror θ_{mech} could be determined by,

$$\theta_{\text{mech}} = \frac{1}{2} \times \tan^{-1}\left(\frac{0.5 \cdot L_{\text{scan}}}{D}\right) \times \frac{180}{\pi} \tag{4}$$

where L_{scan} is the scan length and D is the distance between the screen and DUT. Figures 13(b) and (c) shows mechanical angles measured at different frequencies and driving voltages (5 V$_{\text{pp}}$–20 V$_{\text{pp}}$). Within 5 V$_{\text{pp}}$–20 V$_{\text{pp}}$ driving voltage range, the non-linear dynamic responses due to the spring hardening behavior are observed. At a given driving voltage, the mechanical angle increases with the driving frequency, and will reach a maximum value when the 'jump phenomena' occurs. Due to the spring hardening effect, the driving frequency to induce the maximum mechanical angle is higher than the resonant frequency. In addition, as the driving voltage increases, the maximum mechanical angle and the associate driving frequency will also be increased. The connection structure between the actuator and the mirror plate will be broken when the driving voltage exceeds 20 V$_{\text{pp}}$. Thus, the scanners presented in this study could reach a maximum mechanical angle at the 20 V$_{\text{pp}}$ driving voltage. It is worth to note that
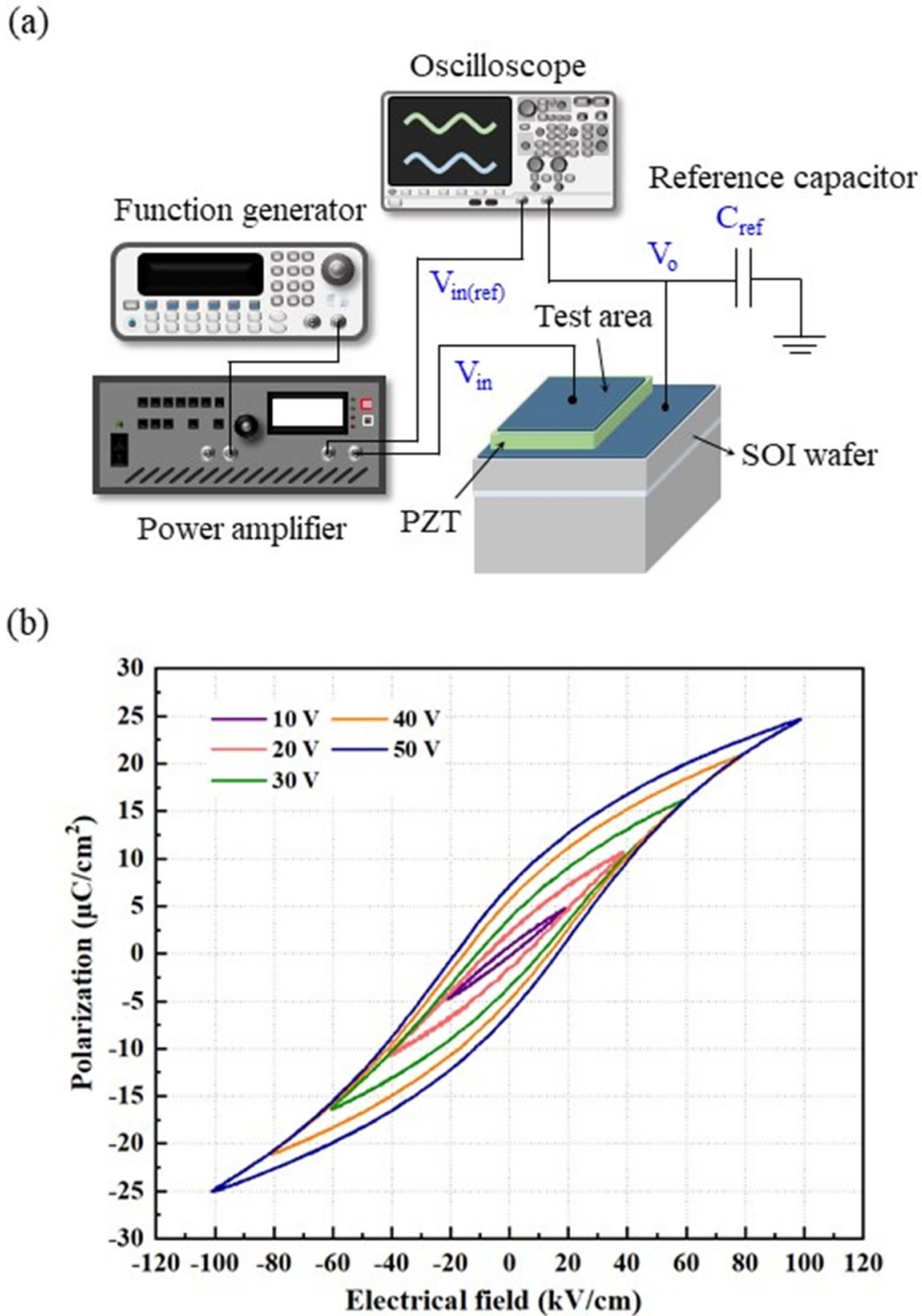
Figure 9. (a) The measurement set up to characterize the *P–E* curve of the PZT thin film used in this study, and (b) the *P–E* curve measured by 0–100 V_{pp} sinusoidal driving signal.

measurements in figure 13(c) indicate the θ_{mech} increases with the driving frequencies until the 'jump phenomena' occurs. However, as depicted in figure 13(b), the increasing of θ_{mech} with the driving frequencies slightly drops when mechanical angle exceeds $\pm 9°$. The results show that the meander curved-beam has lower mechanical stiffness, and hence the actuator

tip will be deformed significantly by the reaction force resulted from the torsional beam when twisting angles exceeding $\pm 9°$. Thus, the stiffness of the actuator is also a design concern to effectively drive the scanning mirror. The measured maximum scanning angles and the related scanning frequencies for the presented two designs are summarized in table 2.
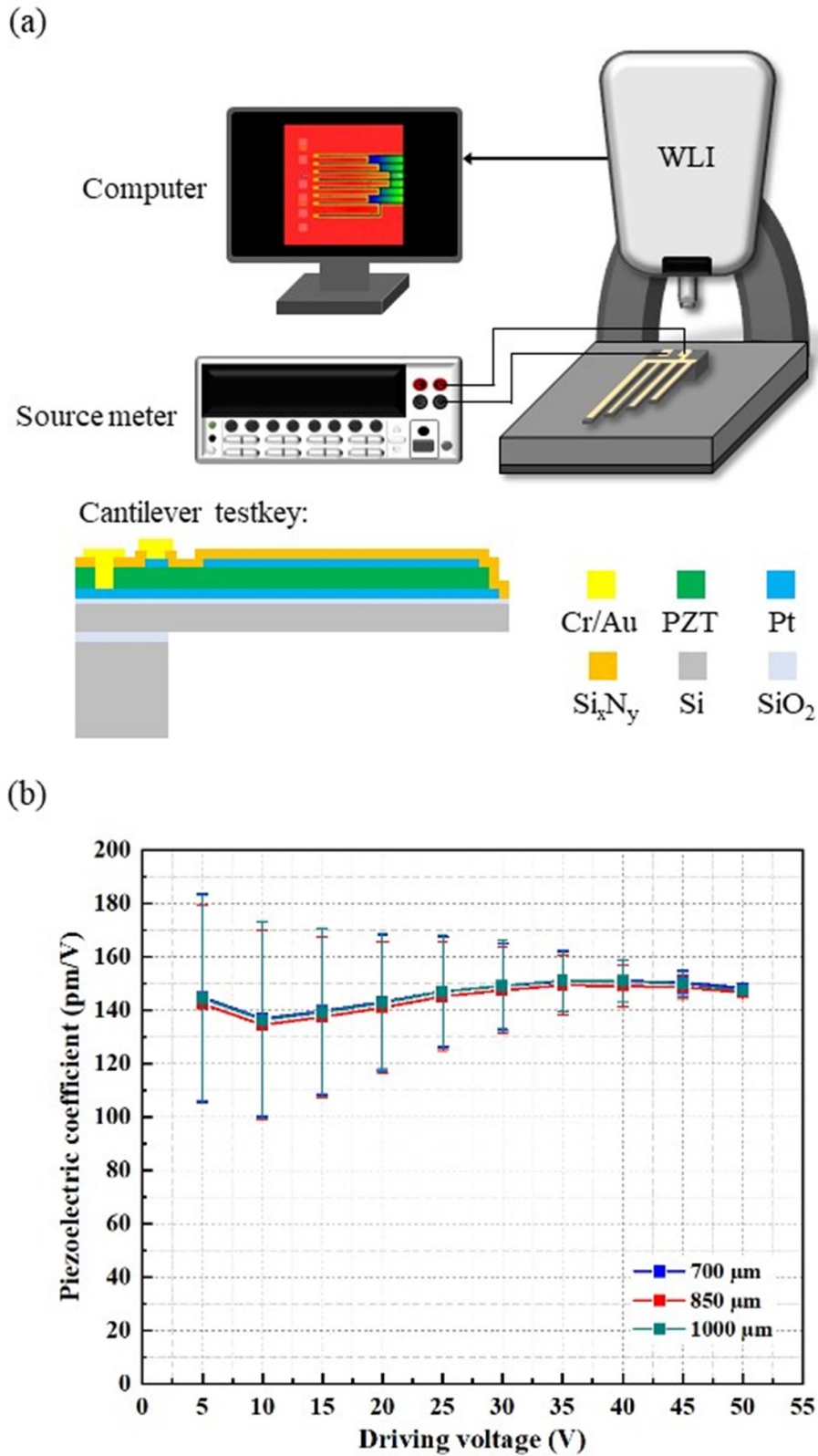
Figure 10. (a) The measurement set up of the load-deflection tests for piezoelectric coefficient d_{31} characterization, (b) the measured d_{31} by applying 5–50 V DC voltages.
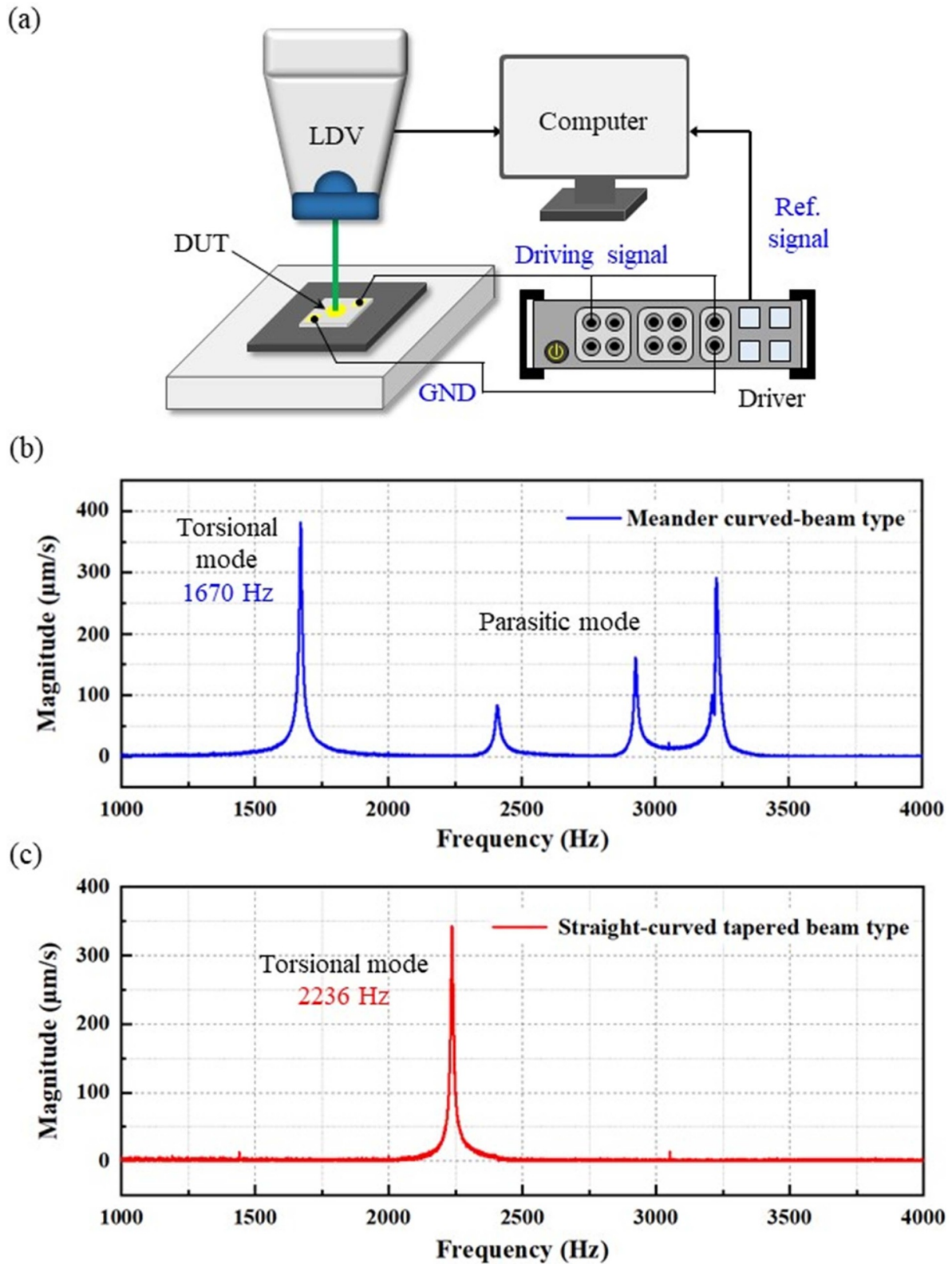
Figure 11. (a) The measurement set up for resonant frequencies of proposed MEMS scanning mirrors, (b) the frequency response of the meander curved-beam design, and (c) the frequency response of the straight-curved tapered beam design.
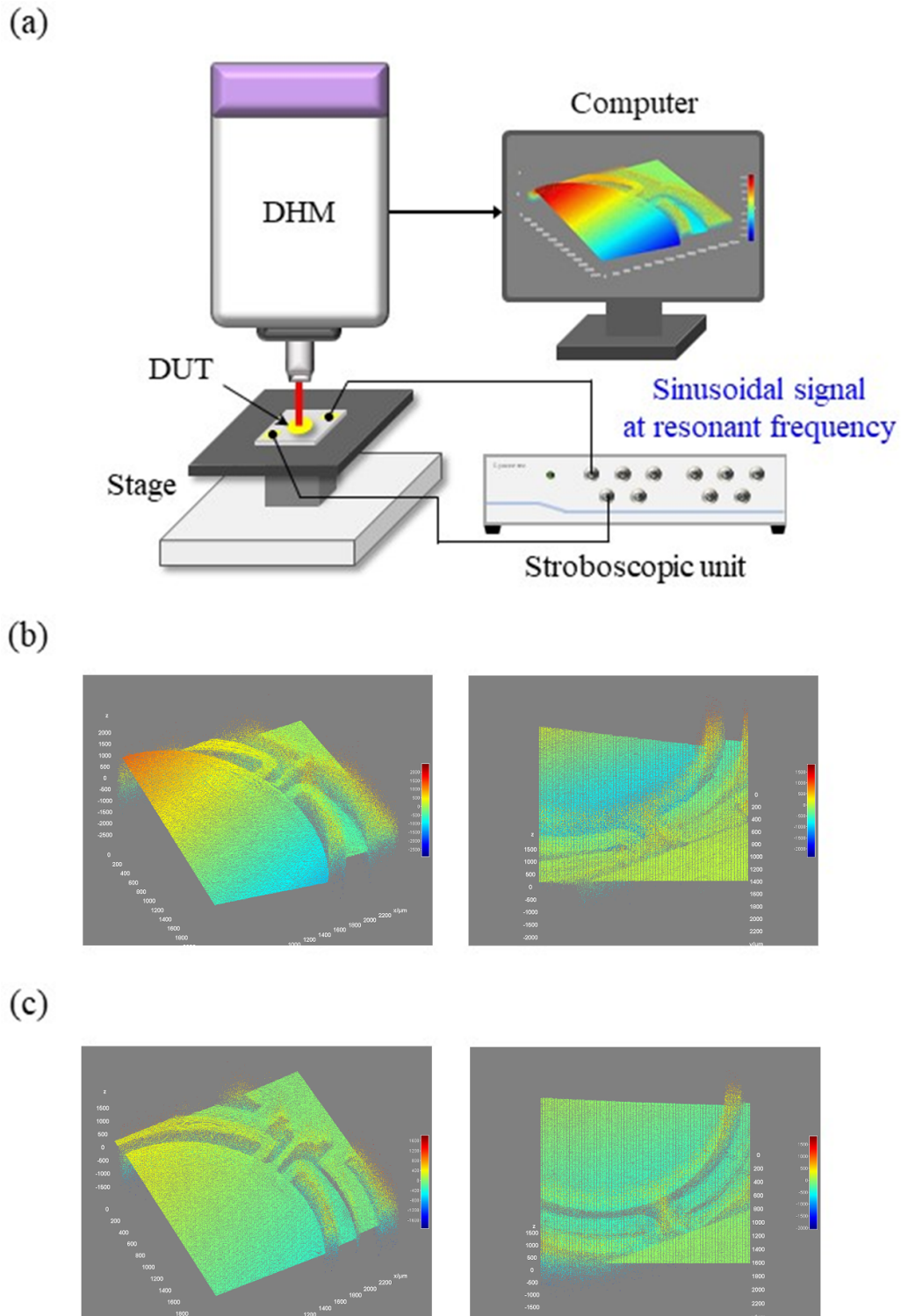
Figure 12. (a) The experiment set up to measure the mode shape, (b) scanning mode shape of the meander curved-beam design, (c) scanning mode shape of the straight-curved tapered beam design.

The driving voltage was 20 V_{pp} unipolar sinusoidal wave signal. Note that the spring hardening effect due to large scanning angle is not considered in the simulation model. Thus, even though the measured d_{31} was higher than the one used in simulation, the measured scanning angles were still close to simulation results in figure 4. Moreover, in comparison, simulations in figure 4 predict the designs could be driven to near $\pm 20°$ mechanical angles. This study further investigated the possible reasons to cause the drop of mechanical angle from $\pm 20°$ to near $\pm 12°–13°$. The zoom-in micrographs captured by the laser confocal microscope in figure 14(a) show the mirror plate and actuator after the broken of scanner. The
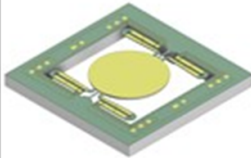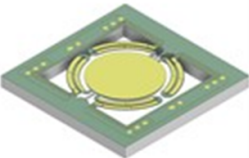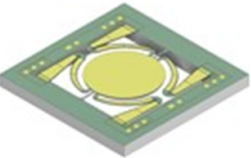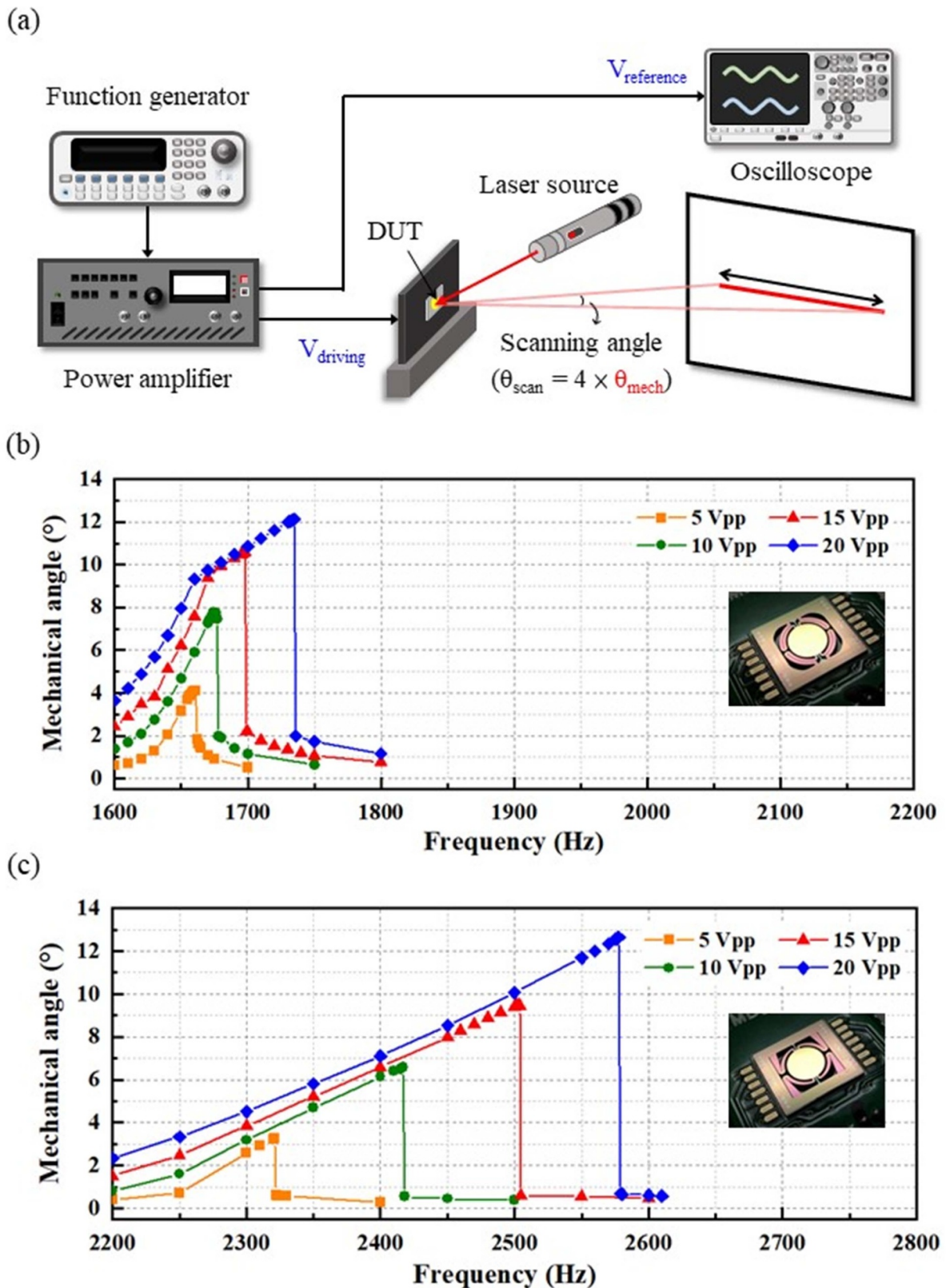
(a)

(b)

(c)

Figure 13. (a) The experiment set up for mechanical angle measurement of proposed MEMS scanning mirrors, (b) measurement results for the meander curved-beam design, and (c) measurement results for the straight-curved tapered design.

Table 2. The comparison of the simulation results according to the maximum allowable stress of Si and the measured maximum scanning angles before failure with 20 V_{pp} driving voltage between reference and proposed MEMS scanning mirror designs.

		Reference	Proposed type (meander curved beam)	Proposed type (straight-curved tapered beam)
Model				
Simulation	Scanning frequency (Hz)	2334	1673	2065
	*Mechanical angle (°)	±20.2 (47 V_{pp})	±20 (31 V_{pp})	±19.8 (30 V_{pp})
	Optical angle (°)	80.4	80	79.2
Measurement	Scanning frequency (Hz)	N/A	1735	2578
	**Mechanical angle (°)	N/A	±12.02 (20 V_{pp})	±12.65 (20 V_{pp})
	Optical angle (°)	N/A	48.1	50.6
	Figure of merit $D_{mirror} \times f_{scan} \times \theta_{scan}$ (mm $\times$ kHz $\times$ °)	N/A	250.4	391.3

*The simulated mechanical angle on the basis of the maximum allowable stress of Si (1.2 GPa)
**The maximum measured mechanical angle before failure

crack on actuator and mirror plate can be observed. In addition, the PZT film distributed on the actuator is depicted in micrographs. Due to the misalignment in processes, the PZT film was not distributed along the fixed-end between actuator and mirror plate. Thus, the stress on the actuator will be significantly increased from ∼0.7 GPa to ∼1.1 GPa, as demonstrated by simulations in figures 14(b) and (c). The results show that the presented designs to pattern the PZT film along the edge of mirror plate would cause the challenge of processes and also bring the risk of high stress on the actuator. It is suggested to pattern the PZT film to align with the edge of top

electrode, as indicated in figure 14(d). In such design, the process alignment on the PZT film has little influence on stress distribution of actuator, as shown in figure 14(e), and hence the scan angle can be significantly improved. In summary, the proposed designs demonstrate the actuator designs to improve the performance of piezoelectric MEMS scanners. In comparison with the two proposed scanners with different actuators, the figure of merit (FoM) determined from the mirror size, scanning frequency, and scanning angle [28] is increased by 56% for the straight-curved tapered beam actuator design.
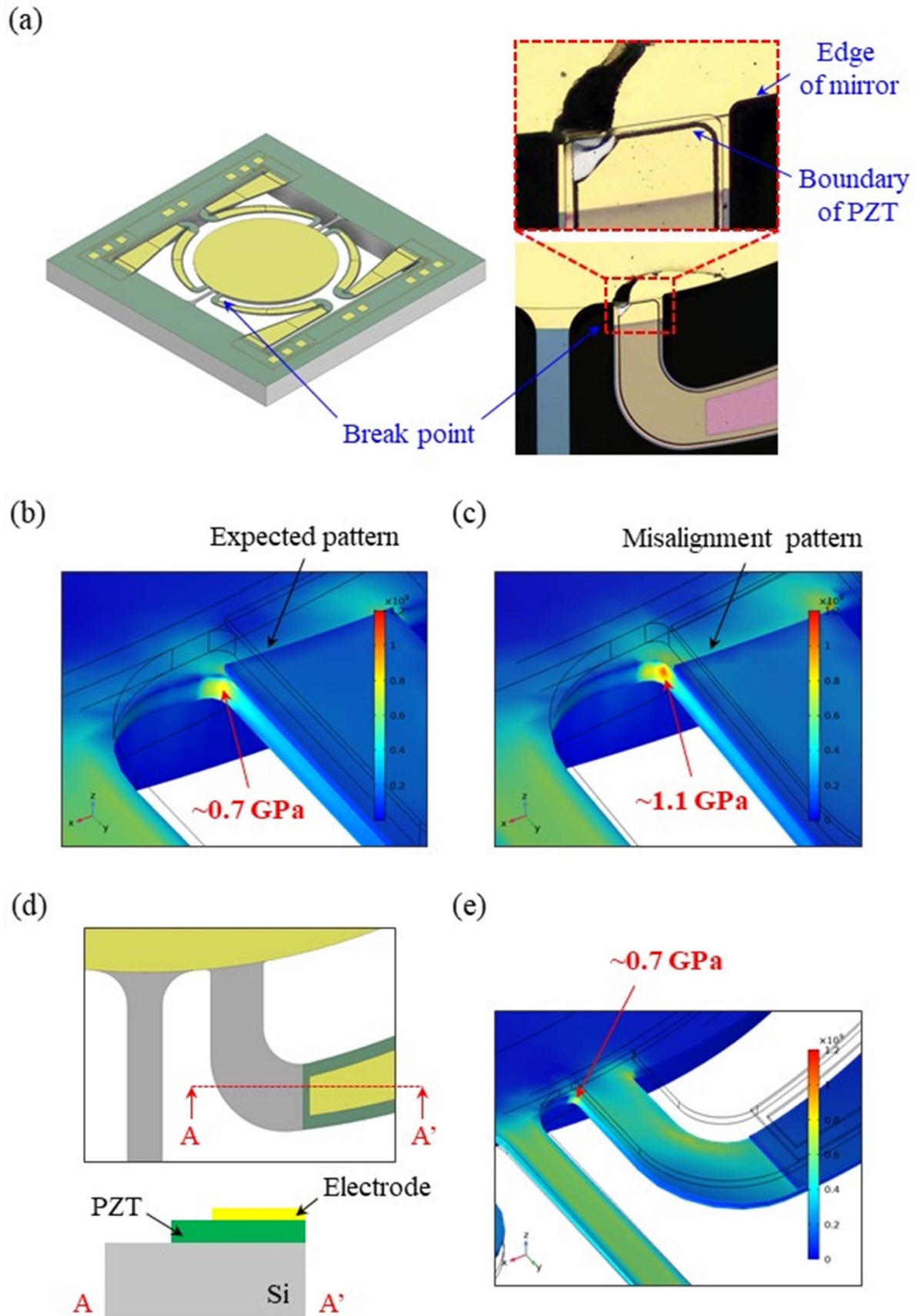
Figure 14. (a) The zoom-in micrographs of the broken actuator, (b) the stress distribution of the idea actuator design with properly aligned PZT film, (c) the stress distribution of the actuator with misaligned PZT film, (d) the suggested PZT pattern to avoid the influence of process alignment issue, (e) the stress distribution near the end of actuator with the suggested PZT pattern.

5. Conclusion

The piezoelectric actuation has shown its potential to realize MEMS scanning mirrors. To meet the requirements of high data collection rate, wide field of view, and long detection range as an automotive LiDAR system, the scanning frequency, scanning angle, and mirror size are three FoMs for the design of MEMS scanning mirrors. Based on the reference piezoelectric MEMS scanning mirror design, this study presents two proposed scanning mirrors with different actuator designs. The reference and proposed scanning mirrors have the same footprint and mirror-plate size. Simulations indicate the proposed scanning mirror with meander curved-beam actuator could significantly increase the scan angle, yet the scanning frequency will drop to below 2 kHz. Thus, performances of such scanning mirror could not meet the specifications for automobile applications. Simulations also depict that the proposed scanning mirror with straight-curved tapered beam actuator could remarkably increase the scan angle and the scanning frequency remains above 2 kHz. In short, the beam length and stiffness are two major design concerns to improve the mechanical scan angle. Moreover, this study also fabricated and tested the two proposed scanning mirrors to demonstrate the feasibility of the designs. The scanners were implemented using the SOI wafer with PZT film. As summarized in table 2, the proposed scanners have the maximum mechanical angles near $\pm 12°$–$13°$. The misalignment of PZT pattern on Si structure significantly increases the stress on actuator, so that the maximum measured mechanical angle is smaller than the simulation one. Thus, the scan angle of the presented devices can be significantly increased by redefined the pattern of PZT film. Moreover, due to the spring hardening effect, the scanning frequencies of proposed designs are higher than their resonant frequencies. Measurements also indicate the straight-curved tapered beam actuator design could enhance the FoM of scanner for about 56%, as compared with the meander curved-beam actuator design. In summary, a piezoelectric MEMS scanning mirrors with 3 mm mirror size and a 2.6 kHz scanning frequency was successfully realized. Meanwhile, the optical scanning angle can reach $50°$ optical angle. Comparing with existing scanners for LiDAR applications [23, 24], the proposed design in this study shows decent performances. Moreover, the presented scanner can be further improved by varying the designs of length and shape of actuator. However, it is also worth it note that the distribution of PZT film on the suspended actuator is a critical design concern.

Data availability statement

All data that support the findings of this study are included within the article (and any supplementary files).

Acknowledgments

ORCID iD

Weileun Fang ⓘ https://orcid.org/0000-0002-6000-026X

References

[1] Druml N, Maksymova L, Thurner T, Lierop D V, Hennecke M and Foroutan A 2018 1D MEMS micro-scanning LiDAR *Proc. Sens. Devices Venice, Italy September 16-20* **9** Cruvinel P, Vieira M, Vieira M A, Zhukov A, Pires I M S, Passaro V M N and Carvalho V pp 48–53

[2] Boni N, Carminati R, Mendicino G, Merli M, Terzi D, Lazarova B and Fusi M 2022 Piezoelectric MEMS mirrors for the next generation of small form factor AR glasses *Proc. SPIE* **12013** 1201305

[3] Yalcinkaya A D, Urey H, Brown D, Montague T and Sprague R 2006 Two-axis electromagnetic microscanner for high resolution displays *J. Microelectromech. Syst.* **15** 786–94

[4] Singh J, Teo J H S, Xu Y, Premachandran C S, Chen N, Kotlanka R, Olivo M and Sheppard C J R 2007 A two axes scanning SOI MEMS micromirror for endoscopic bioimaging *J. Micromech. Microeng.* **18** 025001

[5] Velodynelidar alpha-prime (available at: https://velodynelidar.com/products/alpha-prime/)

[6] Continental 3D flash LiDAR (available at: www.continental-automotive.com/)

[7] Quanergy S Series LiDAR Sensors (available at: https://quanergy.com/products/s3/)

[8] Wu M and Fang W 2004 Design and fabrication of MEMS devices using the integration of MUMPs, trench-refilled molding, DRIE and bulk silicon etching processes *J. Micromech. Microeng.* **15** 535–42

[9] Arslan A, Brown D, Davis W O, Holmstrom S, Gokce S K and Urey H 2010 Comb-actuated resonant torsional microscanner with mechanical amplification *J. Microelectromech. Syst.* **19** 936–43

[10] Ji C-H, Choi M, Kim S-C, Lee S-H, Kim S-H, Yee Y and Bu J-U 2006 An electrostatic scanning micromirror with diaphragm mirror plate and diamond-shaped reinforcement frame *J. Micromech. Microeng.* **16** 1033–9

[11] Yang H, Tang T, Lee S T and Fang W 2007 A novel coilless scanning mirror using eddy current Lorentz force and magnetostatic force *J. Microelectromech. Syst.* **16** 511–20

[12] Weber N, Hertkorn D, Zappe H and Seifert A 2012 Polymer/silicon hard magnetic micromirrors *J. Microelectromech. Syst.* **21** 1098–106

[13] Chen Y-C, Lo S-C, Wang S, Wang Y-J, Wu M and Fang W 2021 On the PZT/Si unimorph cantilever design for the signal-to-noise ratio enhancement of piezoelectric MEMS microphone *J. Micromech. Microeng.* **31** 105003

[14] Cheng H-H, Lo S-C, Huang Z-R, Wang Y-J, Wu M and Fang W 2020 On the design of piezoelectric MEMS microspeaker for the sound pressure level enhancement *Sens. Actuators* A **306** 111960

[15] Filhol F, Defaÿ E, Divoux C, Zinck C and Delaye M T 2005 Resonant micro-mirror excited by a thin-film piezoelectric actuator for fast optical beam scanning *Sens. Actuators* A **123–4** 483–9

[16] Naono T, Fujii T, Esashi M and Tanaka S 2013 A large-scan-angle piezoelectric MEMS optical scanner actuated by a Nb-doped PZT thin film *J. Micromech. Microeng.* **24** 015010

[17] Liu W, Zhu Y, Jia K, Liao W, Tang Y, Wang B and Xie H 2013 A tip–tilt–piston micromirror with a double S-shaped unimorph piezoelectric actuator *Sens. Actuators* A **193** 121–8

[18] Piot A, Pribošek J, Maufay J, Schicker J, Tortschanoff A, Matloub R, Muralt P and Moridi M 2021 Optimization of resonant PZT MEMS mirrors by inverse design and electrode segmentation *J. Microelectromech. Syst.* **30** 216–23

[19] Gu-Stoppel S, Janes J, Kaden D, Quenzer H J, Hofmann U and Benecke W 2013 Piezoelectric resonant micromirror with high frequency and large deflection applying mechanical leverage amplification *Proc. SPIE* **8612** 86120I

[20] Meinel K, Stoeckel C, Melzer M, Zimmermann S, Forke R, Hiller K and Otto T 2021 Piezoelectric scanning micromirror with built-in sensors based on thin film aluminum nitride *IEEE Sens. J.* **21** 9682–9

[21] Lei H, Wen Q, Yu F, Li D, Shang Z, Huang J and Wen Z 2018 AlN film based piezoelectric large-aperture MEMS scanning micromirror integrated with angle sensors *J. Micromech. Microeng.* **28** 115012

[22] AEC documents (available at: www.aecouncil.com/AECDocuments.html)

[23] Fabian S *et al* 2020 Resonant 1D MEMS mirror with a total optical scan angle of 180° for automotive LiDAR *Proc. SPIE* **11293** 1129309

[24] Mendicino G, Merli M, Carminati R, Boni N, Opreni A and Frangi A 2021 Electro-mechanical validation of a resonant MEMS mirror with PZT actuation and PZR sensing *Proc. SPIE* **11697** 1169715

[25] Dekkers M, Boschker H, van Zalk M, Nguyen M, Nazeer H, Houwman E and Rijnders G 2012 The significance of the piezoelectric coefficient $d_{31,eff}$ determined from cantilever structures *J. Micromech. Microeng.* **23** 025008

[26] Lin H Y and Fang W 2003 A rib-reinforced micro torsional mirror driven by electrostatic torque generators *Sens. Actuators* A **105** 1–9

[27] Hsu S, Klose T, Drabe C and Schenk H 2008 Fabrication and characterization of a dynamically flat high resolution micro-scanner *J. Opt. A: Pure Appl. Opt.* **10** 044005

[28] Baran U, Brown D, Holmstrom S, Balma D, Davis W O, Muralt P and Urey H 2012 Resonant PZT MEMS scanner for high-resolution displays *J. Microelectromech. Syst.* **21** 1303–10